Bulletin of the Seismological Society of America, Vol. 101, No. 2, pp. 568–578, April 2011, doi: 10.1785/0120100203

Seismic Noise by Wind Farms: A Case Study from the Virgo Gravitational Wave Observatory, Italy

by Gilberto Saccorotti, Davide Piccinini, Léna Cauchie,* and Irene Fiori

Abstract We present analyses of the noise wave field in the vicinity of Virgo, the Italian–French gravitational wave observatory located close to Pisa, Italy, with special reference to the vibrations induced by a nearby wind farm. The spectral contribution of the wind turbines is investigated using (1) onsite measurements, (2) correlation of spectral amplitudes with wind speed, (3) directional properties determined via multichannel measurements, and (4) attenuation of signal amplitude with distance. Among the different spectral peaks thus discriminated, the one at frequency 1.7 Hz is associated with the greatest power, and under particular conditions it can be observed at distances as large as 11 km from the wind farm. The spatial decay of amplitudes exhibits a complicated pattern, which we interpret in terms of the combination of direct surface waves and body waves refracted at a deep (≈800 m) interface between the Plio-Pleistocenic marine, fluvial, and lacustrine sediments and the Miocene carbonate basement. We develop a model for wave attenuation that allows determining the amplitude of the radiation from individual turbines, which is estimated on the order of 300–400 $\mu\,\mathrm{ms}^{-1}/\sqrt{\mathrm{Hz}}$ for wind speeds over the 8–14 m/s range. On the basis of this model, we then develop a predictive relationship for assessing the possible impact of future wind farm projects.

Introduction

Several detectors are currently operative to reveal the tiny space–time ripples which, according to Einstein's theory of general relativity, are expected in association with astrophysical processes, such as supernova explosions, coalescence of binary systems, and spinning neutron stars.

A class of these gravitational wave detectors (Saulson, 1994) works on the principle of the Michelson interferometer; detectors of this kind are the GEO600 in Germany, the Laser Interferometer Gravitational Wave Observatory (LIGO) in the United States of America, TAMA300 in Japan, and Virgo in Italy (see Data and Resources section). Established under an Italian–French cooperative effort (European Gravitational Observatory, EGO), Virgo is located south of Pisa, about 15 km onshore of the central–northern Tyrrhenian coast (Fig. 1). The Virgo laser interferometer consists of two 3-km-long orthogonal arms oriented N20°E and N70°W, departing from a central building, which also hosts the beam splitter. The return mirrors of the interferometer are located at the extremities of the two arms, hereinafter referred to as the north end and west end. Multiple reflections between these mirrors extend the effective optical length of each arm up to 120 km, thus allowing for sensitivity to spatial strains on the order of $\approx 10^{-22}$ over the 10–10000 Hz frequency range. In order to achieve such extreme sensitivities, the interferometer exploits the most advanced techniques in the field of high-power ultrastable lasers, super-polished mirrors, ultra-high vacuum, and seismic isolation systems (Acernese *et al.*, 2010). Nonetheless, intense low-frequency ground vibrations might overcome the isolation system and deteriorate the detector performances. A major concern is that low-frequency (1–10 Hz) periodic disturbances might match and excite the low-frequency modes of the isolation systems, seriously compromising its functionality. Another concern for Virgo is the noise associated with the tiny fractions of light that exit the interferometer main beam path and are then scattered back by external, seismically excited surfaces (Vinet *et al.*, 1996; Accadia *et al.*, 2010).

By mid-2008, a wind farm composed of four 2-MW turbines was installed approximately 6 km east of Virgo's north end (Fig. 1). Subsequently, plans were submitted to local authorities for adding three additional turbines to the existing wind farm and for installing a new, seven-turbine wind farm at a site located about 5 km west of Virgo's west end. As a consequence, EGO asked the Italian Istituto Nazionale di Geofisica e Vulcanologia to conduct a noise study aiming at verifying properties and intensity of the vibrations produced by the present aerogenerators, with the

*Also at Istituto Nazionale di Geofisica e Vulcanologia, Pisa, Italy.

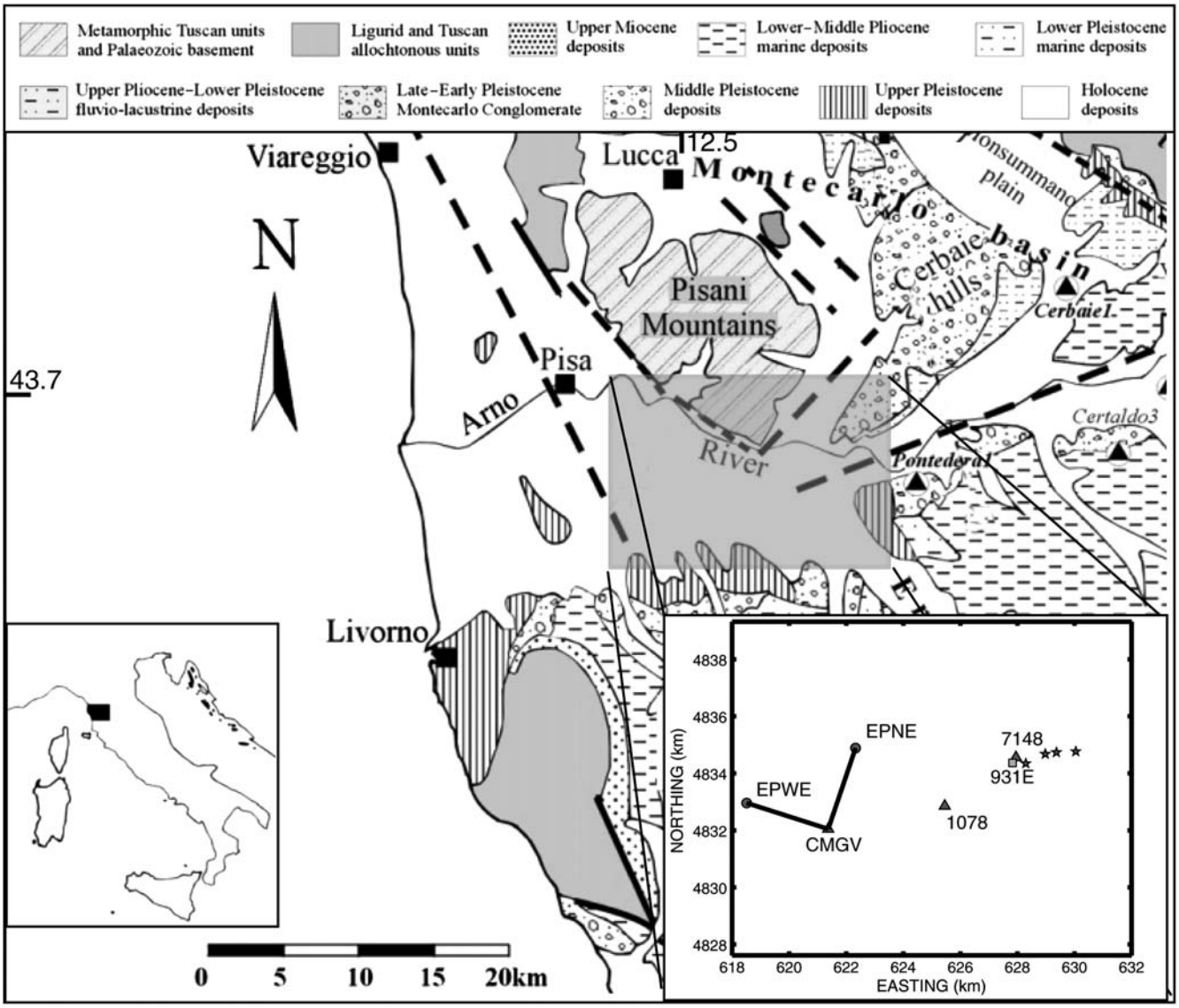

Figure 1 Simplified geological map of western Tuscany. The shaded region marks the area surrounding Virgo and is the object of this study. The inset at the bottom-right shows the configuration of the Virgo antenna (black lines), with location of the recording stations (which were kept fixed throughout the duration of the survey). Circles, EpiSensor accelerometers deployed at Virgo north and west end experimental buildings; triangles, stations equipped with Güralp CMG-40T broadband sensors; square, the reference station 931E, equipped with a Lennartz Le3D-5s seismometer; stars, positions of the four turbines of the wind farm.

ultimate goal of assessing the possible impact of the projected wind farms.

Wind turbines are large and vibrating cylindrical towers strongly coupled to the ground through massive concrete foundations, with rotating turbine blades generating low-frequency acoustic signals.

Vibrations depict a complex spectrum, which includes (1) time-varying frequency peaks directly related to the blade-passing frequency and (2) stationary peaks associated with the pendulum modes of the heavy rotor head and tower and to flexural modes of the tower.

These disturbances propagate via complex paths, including directly through the ground or principally through the air and then coupling locally into the ground. Though weak, such vibrations may be relevant once compared to the local levels of seismic noise. Schofield (2001) found that the intense low-frequency seismic disturbances from the Stateline Wind Project (Washington–Oregon) were well above the local seismic background up to distances of ≈18 km from the turbines. Similar distance ranges were found by Styles *et al.* (2005), who analyzed the possible influence of the Eskdalemuir seismic array, Scotland. Fiori *et al.* (2009) studied the seismic noise generated by a wind farm in proximity of the GEO600 interferometric antenna (Germany) and observed the signal from the turbines up to distances of about 2000 m.

In this work, we present the results from seismic noise analysis in the vicinity of Virgo, with special reference to

the action of the wind farm. The paper is structured into four parts. In the first part (The Study Area and Data Acquisition and Processing sections), we describe the geological setting of the study area and describe the data acquisition procedures. We then describe (in Seismic Noise in Proximity of the Wind Farm) the spectral characteristics of the noise wave field and their relationships with human activities and the wind field. In the third part (Directional Properties and Wave Types and Attenuation with Distance sections), we use small-aperture and large-aperture array deployments to investigate the directional properties of the noise wave field and its amplitude decay with distance from the wind farm. In the last part (Predictive Relationship), we propose an attenuation model involving the combination of direct cylindrical waves propagating at the surface and body waves refracted at a deep (800-m) lithological interface. This attenuation law is eventually used for establishing a predictive relationship for assessing the range of seismic amplitudes that are expected in association with narrowband, shallow sources of noise.

The Study Area

EGO-Virgo is located in the southernmost portion of the Lower Arno river, a Neogenic–Quaternary back-arc basin that formed in the Middle Miocene, during the northern Thyrrenian basin extensional phases (Fanucci *et al.*, 1987; Patacca *et al.*, 1990). This tectonic depression is bounded by the Monti Pisani to the north and by other smooth relief (Monti Livornesi) to the south. The tectonic and climatic pulses during the Miocene allowed marine and continental deposits to overlay the Mesozoic bedrock and the metamorphic Tuscan Unit, previously collapsed along a set of northwest-striking normal faults (Cantini *et al.*, 2001). As a consequence, the top of the carbonatic bedrock deepens from depths of ≈700 m to depths of ≈2500 m as one moves from the eastern to the western sector of the plain (Mariani and Prato, 1988; Della Rocca *et al.*, 1987). The shallow geology (up to depths of ≈60 m) is well documented by a large number of boreholes and surveys, which overall confirm the stratigraphic settings previously described by several authors (e.g., Mazzanti and Rau, 1994; Stefanelli *et al.*, 2008). According to these studies, the deposition due to the glacial activity and the eustatic changes during the Pleistocene fills up the basin with four main layers (Grassi and Cortecci, 2006): (1) conglomerates (conglomerates of the Arno River and Serchio from Bientina) attributed to the Wurm II interglacial period (60–40 ka B.P.); (2) deep mud and fluvio-lacustrine deposits; (3) sands; and (4) shallow mud and fluvio-lacustrine clays.

Data Acquisition and Processing

Our seismic survey had the main goal of discriminating which components of the noise wave field are likely due to the action of the wind generators, in turn determining how these signals propagate and attenuate.

To attain these objectives, we deployed the instruments according to different, time-varying configurations, designed in order to provide the best resolution for both directional and attenuation measurements over a wide frequency band and distance range. In total, we used 14 seismic stations, three of which were kept fixed at the same location throughout the duration of the survey (sites 1078, 7148, and 931E in Fig. 1), while the other three were used for short-duration measurements of site effects via horizontal-to-vertical (H/V) spectral ratios (not described in this paper).

Our instruments consisted of nine RT130-type and five 72A-type recorders from RefTek, each synchronized to the Global Positioning System time signal. All mobile stations used Lennartz LE3D-5s velocimeters exhibiting a flat velocity response over the 0.2–40 Hz frequency band, while two of the three reference sites (1078 and 7148) were equipped with Güralp CMG-40T broadband seismometers with flat velocity response over the 0.025–50 Hz frequency band. For all these instruments sampling rate was set at 125 samples/second/channel. Complementing these data are recordings from two EpiSensor FBA ES-T accelerometers and a further CMG-40 velocimeter located at Virgo's vertexes and central building, respectively. These latter instruments are part of Virgo's internal monitoring network; they are acquired at a rate of 1 KHz and are successively down-sampled at 50 samples/second/channel.

Data acquisition started on 26 October and terminated on 17 November 2009.

Before the data collection, we performed accurate huddle tests between all the possible combinations of recorder–sensor pairs using either noise samples or teleseismic signals to verify the sameness of the amplitude response of the different instruments over the whole frequency band of sensitivity. All the spectra presented throughout the following are either velocity or displacement amplitude spectral densities, derived from the square root of power spectral density estimates as calculated via the Welch (1967) method. Wind data are from an anemometer located atop Virgo's control building, recording wind speed and direction at a rate of 1 datum every 10 s.

Seismic Noise in Proximity of the Wind Farm

Spectral Properties

Seismic noise in proximity of the wind farm exhibits a typical weekly and daily pattern (e.g., the 8-hr workday), as depicted by the spectrogram of Figure 2.

Spectra of human noise span the 1–20 Hz frequency band, as shown in Figure 3, where we compare spectra taken during day-time and night-time intervals in the absence of wind. In general, spectra taken during the day are amplified versions of those collected during the night, indicating

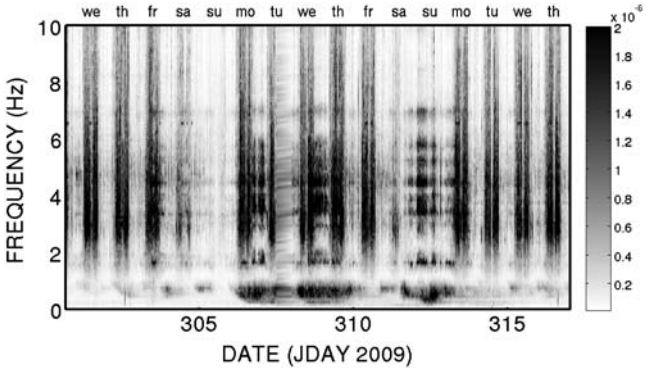

Figure 2. Spectrogram for the vertical component of ground velocity recorded at reference site 931E (Fig. 1). Each spectrogram's column results from the average of spectral estimates obtained over 10 consecutive, nonoverlapping 60-s-long windows of signal. Unit is amplitude spectral density ($ms^{-1}/\sqrt{Hz}$), according to the shaded bar at the right. Labels at the top of the map indicate days of the week; dates are in Julian days.

that no monochromatic signals are generated by human activities.

On the other side, the nightly spectra depict several narrow spectral peaks, the origin of which is not likely related to anthropic noise (e.g., the peak at frequency ≈1.7 Hz on the north–south component and narrow peaks at frequencies ≈3 Hz, 4 Hz, 5.5 Hz, and 7 Hz on the east–west component). As is shown in the rest of this paper, the peak at frequency ≈1.7 Hz of the north–south component is the one which assumes the greatest relevance to the purpose of this study.

Noise Amplitude and Wind Speed

The rows of the spectrogram in Figure 2 are time series of the narrow-band noise amplitude, which we cross-correlate against the contemporaneous time series of wind speed in order to verify whether particular spectral lines are coupled to the action of the wind. The frequency-dependent maxima of the cross-correlation function and associated lag times are shown in Figure 4a,b for the north–south component of motion. Noise exhibits a good correlation with wind speed at several discrete frequencies, centered at approximately 0.45, 1.7, 3.5, and 4.5 Hz.

An example of such correlation is shown in Figure 4c, where the time series of noise amplitude at frequency 1.7 Hz is compared with the chronogram of wind speed. At frequencies above 1 Hz, the correlation peaks of Figure 4a occur at zero lag (Fig. 4b); in other words, noise amplitude grows contemporaneously to the increase of wind speed.

On the contrary, noise amplitude at frequency 0.45 Hz is delayed by several hundred minutes with respect to the wind intensity, suggesting that marine microseism is the most likely

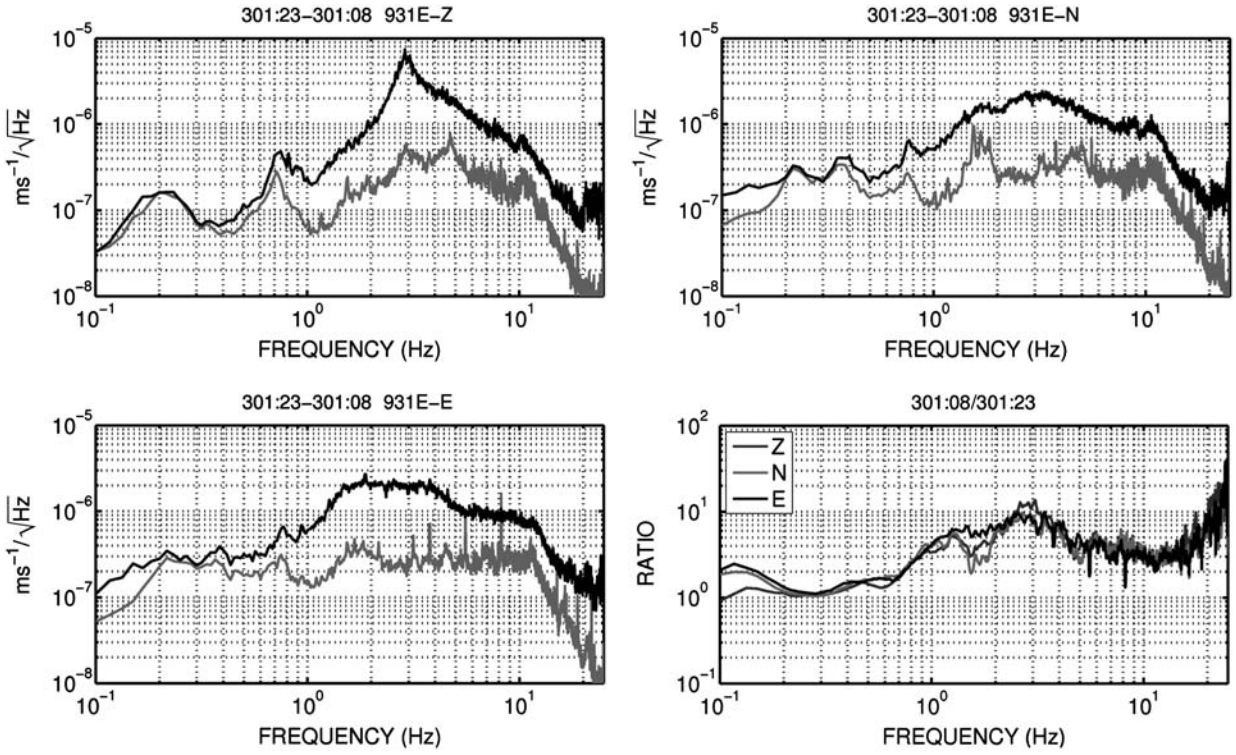

Figure 3. Amplitude spectral density for the three components of ground velocity (Z, vertical; N, north–south; and E, east–west) recorded at reference site 931E (Fig. 1) during night-time and day-time periods (gray and black lines, respectively) in the absence of wind. Spectral densities are obtained using 10 consecutive, nonoverlapping, 600-s-long windows of signal. The bottom right panel reports the spectral ratios between day-time measurements and night-time measurements. The Julian day and hour at the beginning of each recording is indicated above each panel.

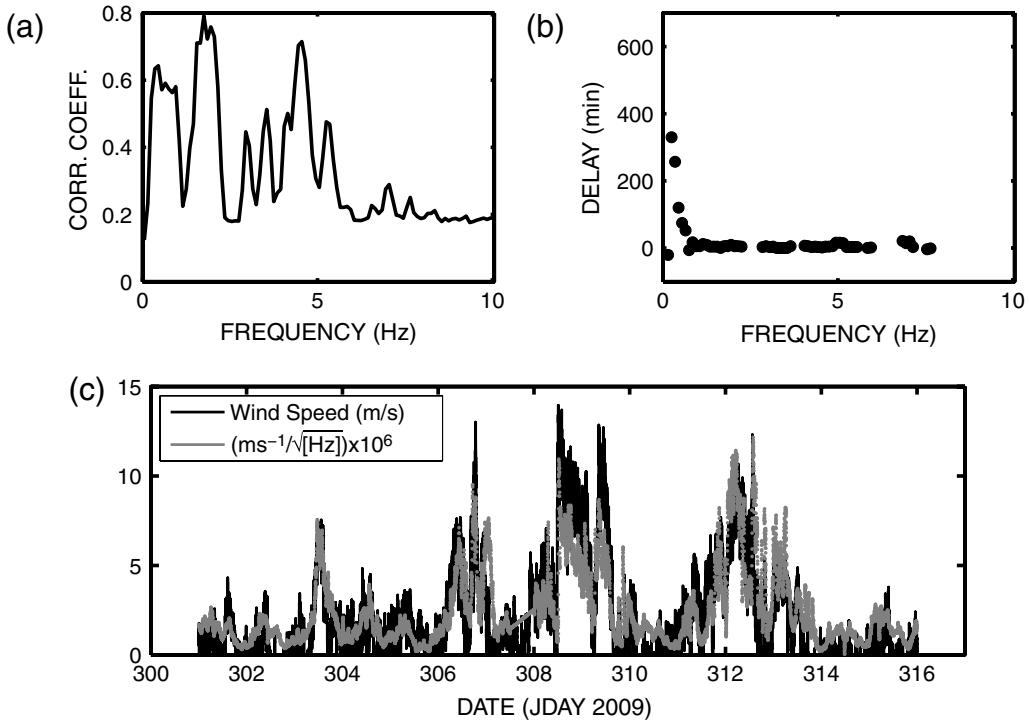

Figure 4. (a) Maxima of the cross-correlation function between narrow-band noise amplitude and wind speed. (b) Time lags associated with correlation coefficients greater than 0.4. (c) Time evolution of the seismic noise amplitude at frequency 1.7 Hz (gray line; north–south component of reference site 931E) and wind speed recorded at EGO's premises (black line).

origin for the seismic noise at that particular frequency. Correlation of seismic noise amplitude with wind speed is well documented by numerous previous studies (e.g., Withers *et al.*, 1996, and references therein). However, all these works indicate that an increase in wind speed affects seismic noise over a wide frequency band (e.g., 1–50 Hz). Our narrow-band correlations are therefore suggestive of a harmonic source, which is itself excited by the action of the wind.

Noise from an Individual Turbine

Figure 5 illustrates the spectrogram for the vertical component of ground velocity recorded in close proximity to an aerogenerator and encompassing a switch-on of the turbine. While the turbine is stopped, we recognize a few transients superimposed to a continuous radiation at frequency 0.45 Hz. We attribute this energy to the eigenoscillation of the tower, which is occasionally excited by adjustments of the nacelle orientation. The switch-on of the turbine is well recognized at about 3000 s into the recording, and it is marked by (1) a few steady spectral lines, the most important of which are at frequencies of 0.45 Hz and 1.7 Hz, and (1) time-varying peaks (gliding spectral lines) at frequencies of about 0.3, 0.6, 0.9...20 Hz and above. The time stationarity of the former peaks indicates that these are likely due to the different modes of oscillation of the tower. Conversely, the gliding spectral lines are attributed to the rotation of the blades, for which the complete period of revolution varies within the 3–10 s range as a function of wind speed and nacelle orientation. Figure 6 compares spectra from beneath the turbine (taken at low wind speeds) with noncontemporaneous spectra observed at the reference site 931E during a 1-hr-long period of strong wind. The two sets of spectra are markedly different, and the only common peak is found at the vertical and

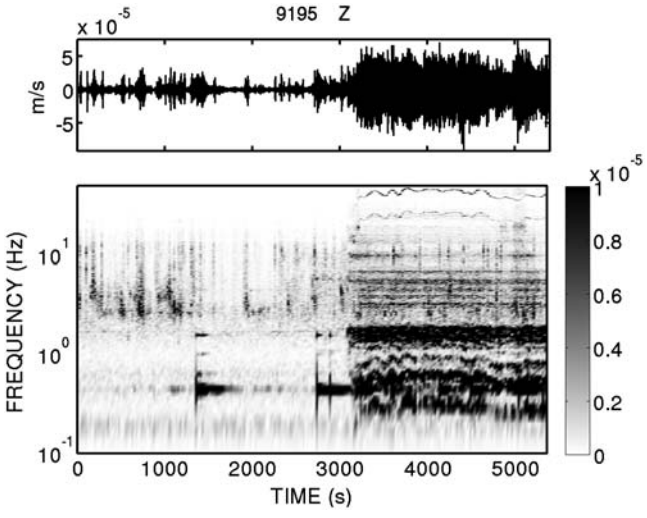

Figure 5. Time series (top) and corresponding spectrogram (bottom) for the vertical component of ground velocity (Z) observed at the base of a turbine and encompassing a switch-on sequence (≈3100 s into the record). Unit is amplitude spectral density ($ms^{-1}/\sqrt{Hz}$, according to the gray scale at the right.

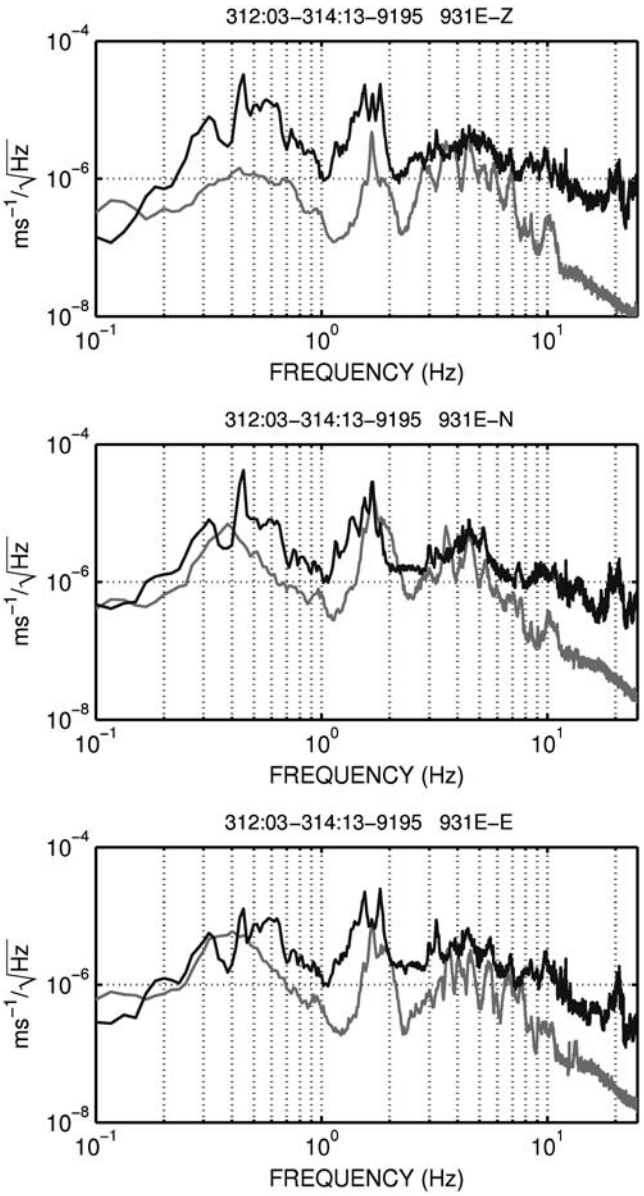

Figure 6. Comparison of spectral amplitudes observed beneath a turbine and at reference site 931E (black and gray lines, respectively). The two data sets are not simultaneous and correspond to wind speed of ≈3 m/s and ≈11 m/s, respectively.

north–south components of motion, at frequency 1.7 Hz. This suggests that either the other peaks that we found to correlate clearly with wind speed (e.g., 3.5, 4.5 Hz…) are not related to the action of the wind farm or that path effects, and the combination of waves radiated from individual turbines, severely modify the spectral composition of the seismic noise as it propagates away from the wind farm.

As a consequence, beneath-turbine measurements cannot be taken as representative of the overall wind farm noise as observed in the far field. The next two sections are thus dedicated to finding indirect evidences for determining the noise spectral components that are actually due to the action of the wind farm.

Directional Properties and Wave Types

We use a dense, two-dimensional array deployment installed about 480 m from the closest turbine to investigate the composition of the noise wave field around the wind farm. Under the plane-wave approximation, we use interstation delay times measured via cross correlation to derive the two components of the horizontal slowness vector and, hence, the apparent velocity and back azimuth for waves impinging at the array (Del Pezzo and Giudicepietro, 2002). Multichannel data streams are first passed through a bank of 0.2-Hz-wide band-pass filters spanning the 0.1–5.1 Hz frequency band; for each frequency band, interstation cross correlations are calculated using nonoverlapping, 600-s-long windows of signal, thus allowing for time-dependent and frequency-dependent estimates of the kinematic properties of the noise wave field. We decided to use such long time windows because we noted correlation estimates became stable for time windows longer than ≈500 s.

The results (Fig. 7) clearly indicate that most of the energy at frequencies above 1 Hz propagates from directions that are compatible with the wind farm (back azimuths between 90° and 110°). Conversely, waves at frequencies below 1 Hz mostly come from the coast (i.e., back azimuths pointing to the west), confirming that marine microseism is the most powerful source over this particular frequency range.

Our measurements also indicate a marked dispersion, indicating a dominance of surface waves. Phase velocities range from 1000–2000 m/s below 1 Hz to 100–200 m/s at frequencies above 2 Hz. These values are consistent with those listed by Castagna *et al.* (1985) for shear waves propagating in saturated, unconsolidated sediments. At 1.7 Hz, particle motions at the array site are mostly horizontal and oriented north–south (i.e., perpendicular to the direction of propagation), thus suggesting a dominance of Love waves.

Attenuation with Distance

Figure 8 illustrates the spatial decrease of spectral amplitudes as a function of distance from the wind farm. Measurements are taken during a windy night (wind speed ≈14 m/s), for which we do expect low intensity of human source microseisms and high radiation from the wind turbines.

Several of the frequency peaks that correlate well with wind speed (e.g., 1.7, 3.5, and 4.5 Hz on the north–south component) attenuate as distance from the wind farm increases, thus reinforcing the hypothesis that these peaks are due to the action of the turbines. In particular, the peak at 1.7 Hz also is clearly observed at Virgo's west end, about 11 km from the energy plant.

For this particular frequency, the decay of spectral amplitude with increasing distance from the source exhibits a complicated pattern (Fig. 8b). In particular, we observe

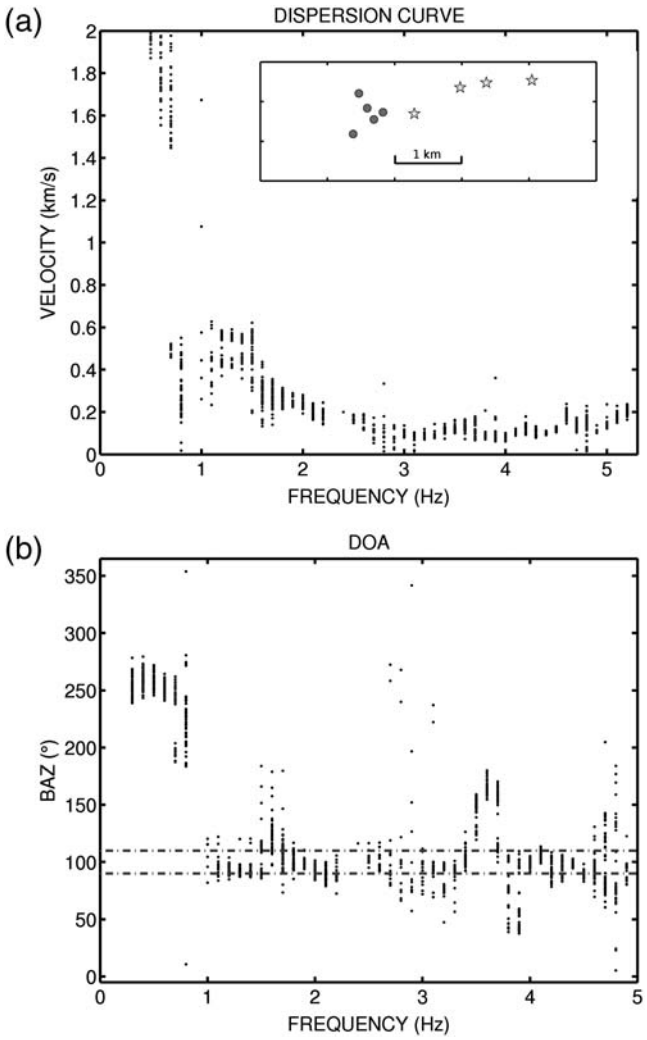

Figure 7. (a) Dispersion curve derived from the frequency-dependent slowness estimates. Slowness data are obtained from 24 consecutive, nonoverlapping, 600-s-long time windows. The inset shows the configuration of the array used for slowness estimates (circles), with respect to the wind farm (stars). (b) Wave back azimuth (BAZ; direction-of-arrival) as a function of frequency. The two dashed lines mark the angular interval encompassing the wind farm.

a marked change in the amplitude decay rate for source-to-receiver distances on the order of 2500–3000 m.

A simplified propagation model explaining the two different attenuation rates involves the combination of direct surface waves and body waves propagating along deeper paths, the latter being characterized by higher velocities and quality factors.

In this model, if we assume an isotropic source located at the free surface, the amplitude of the surface waves $A_D(f, r)$ scales with distance r according to a general attenuation law for cylindrical waves (e.g., Del Pezzo *et al.*, 1989):

$$A_D(f, r) = \frac{A_0}{\sqrt{r}} e^{-\frac{\pi f r}{Q_0 v_0}}, \qquad (1)$$

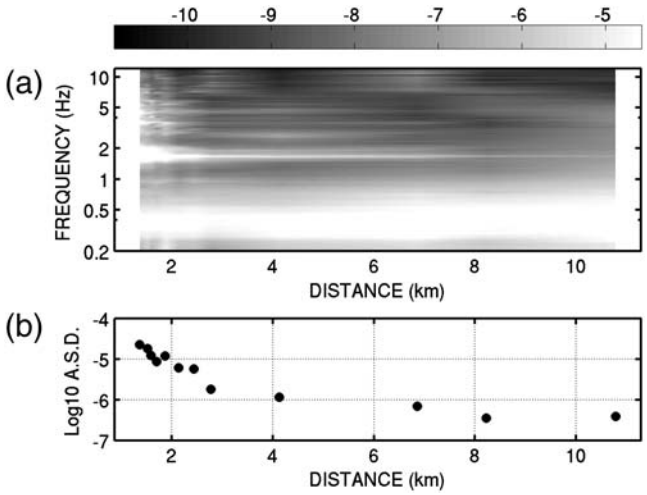

Figure 8. (a) Spatial decay of the amplitude of ground velocity (north–south component) for increasing distance from the barycenter of the wind farm. The image map is the logarithm of the amplitude spectral density ($\mathrm{ms}^{-1}/\sqrt{\mathrm{Hz}}$), according to the shaded bar at the top. The peak at 1.7 Hz is clearly observed at Virgo's west end, ≈11 km from the wind farm. (b) Spatial decay of amplitude spectral densities (A.S.D.) at 1.7 Hz. The decay rate changes abruptly for distances on the order of 2500–3000 m, suggesting the emergence of waves that propagated through deeper paths.

where A_0 is the seismic amplitude at the source, f is the frequency, and (Q_0, v_0) are the quality factor and surface-wave velocity of the shallowest layer, respectively.

We simplify the propagation of the body waves in terms of head waves refracted at a deep (≈800 m) interface between the shallow Plio-Pleistocenic sediments and the Miocene carbonates (Fig. 9). The downgoing and upgoing ray segments of these waves traverse an 800-m-thick layer of average quality factor and shear-wave velocity (Q_1, v_1), respectively, and are continuously refracted at the interface with a half-space of quality factor and velocity (Q_2, v_2).

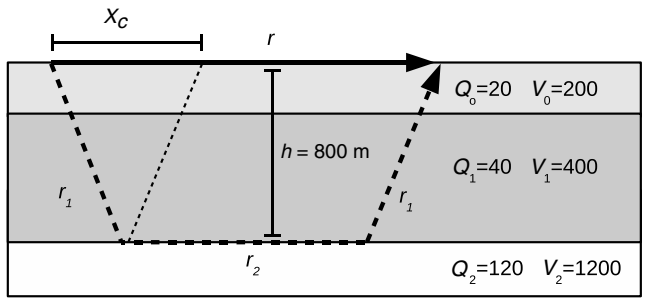

Figure 9. Sketch of the propagation model used for interpreting amplitude data. Seismic waves radiated from a source at the surface propagate as both surface waves and body head waves refracted at a deep interface; X_C is the critical distance. Surface waves are entirely confined within the shallowest layer, while body waves propagate through a layer of thickness h and at the interface between this layer and a half-space represented by the carbonate basement. Shear-wave velocities (V_n) and quality factors (Q_n) are listed within each layer.

Neglecting the short propagation paths throughout the shallowest layer, the attenuation with distance of these body waves is thus described by the relationship

$$A_R(f, r) = A_0(2r_1 + r_2)^{-n} e^{\frac{-2\pi r_1 f}{Q_1 v_1} - \frac{\pi r_2 f}{Q_2 v_2}}, \quad (2)$$

where n is the geometrical spreading coefficient, which, for body waves, is expected to take unit value.

Thus, for an observer recording the signal from N turbines which vibrate with the same amplitude A_0 and are located at distances r_i, $i = 1 \ldots N$, the amplitude is given by the sum of equation (1) and equation (2):

$$A_T(f) = A_0 \sum_{i=1}^{N} [A_D(f, r_i) + A_R(f, r_i)], \quad (3)$$

remembering, however, that the A_R term (equation 2) is not defined for horizontal distances r shorter than the critical distance.

Equation 3 is based on the critical assumptions that (1) each turbine radiates a signal of the same amplitude; (2) these signals propagate in phase, thus constructively interfering throughout their paths, and (3) the energy is equally parted into surface-wave and body-wave ray paths.

The free parameters in equation (3) are the velocities and quality factors v_i, $Q_i (i = 0, \ldots 2)$, of the two layers and the half-space, the geometrical spreading coefficient n of the body head waves, and the amplitude A_0 of the radiation from each individual turbine. The depth to the top of the carbonate basement h is rather well constrained by well-log data; and, as specified previously, it is assumed to take the value of 800 m.

For fitting equation (3) to data, we first consider a sample set of amplitude versus distance measurements obtained over 1-hr-long recording at 14 three-component stations. For these signals, we average the amplitude spectral densities over a 0.1-Hz-wide frequency band encompassing the reference frequency of 1.7 Hz and eventually obtain three-component amplitudes from the quadrature sum of spectra derived at the individual components of ground motion.

The fit is conducted using an exhaustive grid search in which all the free parameters in equation (3) are allowed to vary over appropriate ranges. For A_0 and n, we used 11 values spanning the 10–1000 $\mu\,\mathrm{ms}^{-1}/\sqrt{\mathrm{Hz}}$ and 0.5–1 ranges, respectively. The three $Q_i \times v_i (i = 0 \ldots 2)$ products were instead allowed to vary over an $11 \times 11 \times 11$ grid spanning the [3000,5000], [10000,80000], and [100000, 200000] m/s intervals, respectively. These ranges encompass S-wave velocity and quality factor values that are expected in association with the shallow geology of the site (e.g., Castagna, 1985; Campbell, 2009). For each combination of these parameters, we then calculate the L_1 misfit function

$$L_1(\mathbf{m}) = \sum_{i=1}^{N_{\mathrm{obs}}} |A^{\mathrm{obs}}(r_i) - A^{\mathrm{pre}}(r_i)|, \quad (4)$$

where $\mathbf{m}$ is a model vector containing the parameters $(A_0, n, Q_0V_0, Q_1V_1, Q_2V_2)$, and A^{obs}, A^{pre} are the observed amplitudes and those predicted in the sense of equation (3). From this procedure, we noted that the misfit function (equation 4) is mostly sensitive to the source amplitude and body-wave spreading coefficient. Therefore, we assigned the values reported in Figure 9 to seismic velocities and quality factors and inverted amplitude observations only for the spreading coefficient of body waves and the amplitude at the source. The inversion was separately applied to amplitude data taken from twenty 1-hr-long intervals of noise recorded by different network geometries, at distances from the barycenter of the wind farm ranging from 1200 m to ≈11000 m. For each set of measurements, we only considered stations for which the peak at 1.7 Hz was clearly visible. Best-fitting values of A_0 and n were sought over a 21×21 regular grid spanning the same intervals mentioned previously.

Figure 10 shows the L_1 error function from a sample data set, and the comparison between the observed amplitudes and those predicted on the basis of the minimum-norm model.

The sample error function of Figure 10a indicates a clear correlation between A_0 and n. Nonetheless, results from the whole set of inversions depict narrow distributions, thus supporting the overall robustness of the estimates. In fact, mean values and $\pm 1\sigma$ uncertainties for the A_0/A_{rif} ratio (where A_{rif} is the amplitude at reference site 931E) and the spreading coefficient n are 29.9 ± 1.9 and 0.70 ± 0.04, respectively.

The geometrical spreading coefficient of head waves is sensitively smaller than the unit value that is expected for body waves. This occurrence is likely due to the fact that our simplified model assumes that the source radiates isotropically, in turn neglecting the additional conversion to surface waves as body waves impinge at the Earth's surface.

Predictive Relationship

The points discussed in the preceding sections allow the establishment of a predictive relationship for assessing the effects of future wind farms with custom turbine configuration. As a first step, we use the results from the inversion of amplitude data to convert the seismic amplitude observed at the reference site to the radiation amplitude at unit distance from a single turbine.

In order to relate these amplitudes to the wind speed, we consider that the energy in a volume of air goes as the square of its velocity and that the volume that passes by the turbine per unit time increases linearly with wind velocity.

Thus, the available power P at an individual turbine is proportional to the cube of the wind velocity W ($P \propto W^3$).

By further assuming that the power in the seismic signal is proportional to the wind power available to the turbine, it turns out that the signal amplitude goes as the wind velocity to the 3/2 power (Schofield, 2001; Fiori *et al.*, 2009). We

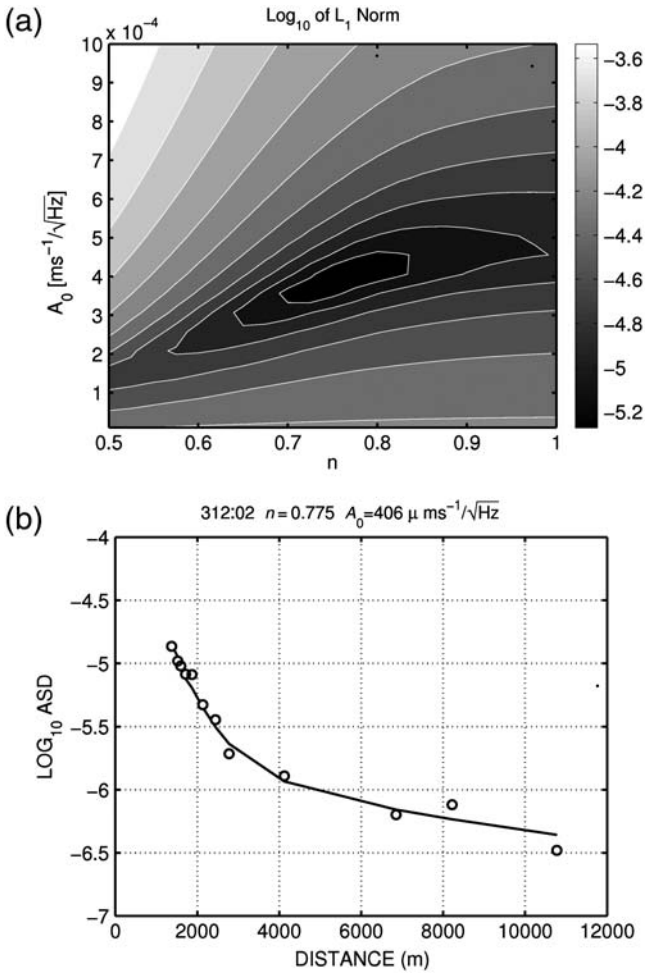

Figure 10. (a) L1-norm misfit function obtained from the regular grid-search over the parameters A_0 and n for fitting equation 3 to three-component amplitude data. (b) Fit of experimental, three-component amplitudes using the best values of the parameters obtained from the minimum of the misfit function in (a).

thus plot the single-turbine amplitudes against the wind speed for the entire observation period and fit these data with a power law in the form

$$A_s = c + a \cdot W^{\frac{3}{2}}, \tag{5}$$

where A_s is the amplitude spectral density of the ground velocity (in $\mathrm{ms}^{-1}/\sqrt{\mathrm{Hz}}$) at unit distance from a single turbine, and W is the wind speed in m/s (Fig. 11). The best-fitting parameters are $a = 2.13 \times 10^{-7}$ $\mathrm{Hz}^{-0.5}$ and $c = 1.40 \times 10^{-6}$ ms^{-1} $\mathrm{Hz}^{-0.5}$. The fit is not very well constrained, likely as a result of a combination of several causes, such as contamination of the seismic signal by additional noise sources and a difference of the wind field between Virgo's anenometer and that of the wind farm.

Keeping these limitation in mind, one can substitute the A_0 of equation (3) with the right-hand side of equation (5), thus deriving the expected spatial distribution of ground vibration amplitudes as a function of wind speed for any custom configuration of wind turbines. Once a robust set of statistics of wind speed becomes available, these data eventually will allow the derivation of shake maps that describe the probability of exceeding given ground-motion amplitudes throughout the study area. Moreover, in this application, it must be considered that the wind speed measured at Virgo's anenometer (placed at ≈10 m height) is expected to be significantly smaller than that at the blades' elevation (60–100 m).

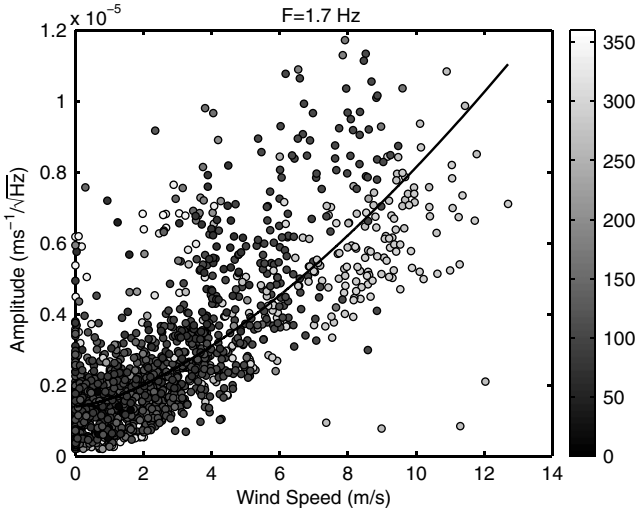

Figure 11. Relationships between vibration amplitude at a single turbine and wind speed. Gray tones indicate wind directions measured clockwise from the north (see gray scale at the right).

Discussion and Conclusion

In this paper we analyzed the seismic noise wave field in the vicinity of the Virgo gravitational wave observatory (Cascina, Pisa—Italy), with special reference to the action of a nearby wind farm composed by four 2-MW turbines. Using stations deployed at distances ranging between ≈1200 m and ≈11, 000 m from the barycenter of the wind farm, we obtained recordings of the noise wave field over a wide range of site conditions and epicentral ranges. We noted that path effects significantly modify the source spectrum, implying that beneath-turbine measurements are not fully indicative of the effective contribution of the wind farm to the far-field ground vibration spectra. Therefore, the spectral components of the noise wave field that likely are due to the action of the wind farm had to be discriminated on the basis of indirect evidences, including (1) correlation of narrow-band noise amplitude with wind speed, (2) directional properties, and (3) attenuation with increasing distance from the wind farm.

Basing on these results, we individuated several frequency bands that are likely due to the action of the wind farm. Among these, the most energetic is that at frequency 1.7 Hz, which, under particular conditions (i.e., low cultural

noise and strong wind), can be clearly observed at epicentral distances as large as 11 km.

At this particular frequency, waves depict a complicate pattern of attenuation with distance, characterized by a marked decrease in the decay rate for ranges larger than 2500–3000 m.

We interpreted this pattern in terms of a simplified propagation model involving the combination of direct, cylindrical waves and body head waves continuously refracted at a deep (≈800 m) interface separating the shallow marine–lacustrine sediments from the carbonate basement. This model is based on several simplifying assumptions, including: seismic energy is equally parted into surface and head body waves, and no other wave types and/or wave conversions are allowed; and site effects are negligible.

By further assuming that (1) each turbine radiates the same amount of energy, (2) signals from individual turbines sum constructively, (3) the velocity structure of the propagation medium is laterally homogeneous, and (4) local amplification effects are negligible, we thus defined a model relating the seismic amplitude recorded at a given distance to the radiation of each individual turbine.

Assumption (2) is likely to provide an overestimation of the radiation amplitude from individual turbines. A more realistic estimates should consider that the turbines are not all in phase and are not operating at exactly the same frequency because of the slight possible variations in rotation speed and wind conditions across the farm. These are quasi-random sources and therefore add in quadrature, so they are not linear, as previously assumed. Therefore, 100 turbines are 10 times as noisy as 1, not 100 times; thus, because we are dealing with a farm composed of four turbines, the noise consideration would imply scaling the estimated single-turbine amplitudes by about a factor of 2, which is probably not so relevant once compared to the assumptions reported at points (3) and (4) (i.e., site and path effects).

Separately, we also found a relationship between wind speed and noise amplitude that is reasonably well-fitted by a power law. Therefore, these two pieces of information allow us to build a predictive relationship linking wind speed with expected noise amplitude for any custom configuration of turbines. Given a robust statistics of wind speed, this latter argument will permit assessment of the probabilities of exceeding an arbitrary noise amplitude threshold at any site of interest within the study area, as a consequence of present or projected wind farms.

Data and Resources

Additional information about gravitational wave detectors that work on the principle of the Michelson interferometer may be obtained from *The Virgo collaboration, Virgo Final Design 1997 VIR-TRE-DIR-1000-13*, available at https://tds.ego-gw.it/itf/tds/ (last accessed January 2011).

All data used for this study are property of the EGO Consortium and cannot be released to the public.

Acknowledgments

Thoughtful revisions from Martin C. Chapman, Salvatore de Lorenzo, and an anonymous reviewer greatly contributed to improving the quality of the manuscript. The research was fully supported by the European Gravitational Observatory Consortium. Thomas Braun, Riccardo Azzara, Nicola Piana Agostinetti, Chiara Montagna, and Luciano Zuccarello participated in the field survey. Federico Paoletti provided superb logistical assistance during the data acquisition. Finally, we are grateful to Jacques Colas, whose constructive criticism greatly stimulated the conduction of the research.

References

Acernese, F., F. Antonucci, S. Aoudia, K. G. Arun, P. Astone, G. Ballardin, F. Barone, M. Barsuglia, T. S. Bauer, and M. G. Beker, *et al.* (2010). Measurements of Superattenuator seismic isolation by Virgo interferometer. *Astropart. Phys.* **33,** 182–189.

Accadia, T., F. Acernese, F. Antonucci, P. Astone, G. Ballardin, F. Barone, M. Barsuglia, T. S. Bauer, M. G. Beker, and A. Belletoile, *et al.* (2010). Noise from scattered light in Virgo's second science run data, *Classical Quant. Grav.* **27,** no. 19, doi 10.1088/0264-9381/27/19/194011.

Campbell, K. W. (2009). Estimates of shear-wave Q and k_0 for unconsolidated and semiconsolidated sediments in eastern North America, *Bull. Seismol. Soc. Amer.* **99,** no. 4, 2365–2392, doi 10.1785/0120080116.

Cantini, P., G. Testa, G. Zanchetta, and R. Cavallini (2001). The Plio-Pleistocene evolution of extensional tectonics in northern Tuscany, as constrained by new gravimetric data from the Montecarlo basin (lower Arno Valley, Italy), *Tectonophysics* **330,** 25–43.

Castagna, J. P., M. L. Batzle, and R. L. Eastwood (1985). Relationships between compressional-wave and shear-wave velocities in clastic silicate rocks, *Geophysics* **50,** 571–581.

Del Pezzo, E., and F. Giudicepietro (2002). Plane wave fitting method for a plane, small aperture, short period seismic array: A MATHCAD 2000 professional program, *Comput. Geosci.* **28,** 59–64.

Del Pezzo, E., G. Lombardo, and S. Spampinato (1989). Attenuation of volcanic tremor at Mt. Etna, Sicily, *Bull. Seismol. Soc. Amer.* **79,** 1989–1994.

Della Rocca, B., R. Mazzanti, and E. Pranzini (1987). Studio geomorfologico della Pianura di Pisa, *Geografia Fisica e Dinamica Quaternario* **10,** 56–84.

Fanucci, F., M. Firpo, and A. Ramella (1987). Genesi ed evoluzione di piane costiere del Mediterraneo: Esempi di piccole piane della Liguria, *Geografia Fisica e Dinamica Quaternario* **10,** 193–203.

Fiori, I., L. Giordano, S. Hild, G. Losurdo, E. Marchetti, G. Mayer, and F. Paoletti (2009). A study of the seismic disturbance produced by the wind park near the gravitational wave detector GEO-600, *Proc. 3rd Int. Meeting on Wind Turbine Noise*, Aalborg, Denmark, 17–19 June 2009.

Grassi, S., and G. Cortecci (2005). Hydrogeology and geochemistry of the multilayered confined aquifer of the Pisa plain (Tuscany-central Italy), *Appl. Geochem.* **20,** 41–54.

Mariani, M., and R. Prato (1988). I bacini neogenici costieri del margine tirrenico: Approccio sismicostratigrafico, *Memorie della Società Geografica Italiana* **41,** 519–531.

Mazzanti, R., and A. Rau (1994). La geologia, in *La pianura di Pisa e i rilievi contermini. La natura e la storia*, Mazzanti, R. (Ed.), *Memorie della Società Geografica Italiana* **50,** 31–87.

Patacca, E., R. Sartori, and P. Scandone (1990). Tyrrhenian basin and Apenninic arcs: Kinematic relations since Late Tortonian times, *Memorie della Società Geografica Italiana* **45,** 425–451.

Saulson, P. R (1994).*Fundamentals of Interferometric Gravitational Wave Detectors*, World Scientific Publishing, Singapore, 316 pp.

Schofield, R. (2001). *Seismic Measurements at the Stateline Wind Project*, Rept. no. LIGO T020104-00-Z, Laser Interferometer Gravitational Wave Observatory, 28 pp., available at http://www.ligo.caltech.edu/docs/T/T020104-00.pdf (last accessed January 2011).

Stefanelli, P., C. Carmisciano, F. Caratori Tontini, L. Cocchi, N. Beverini, F. Fidecaro, and D. Embriaco (2008). Microgravity vertical gradient measurement in the site of VIRGO interferometric antenna (Pisa plain, Italy), *Ann. Geophys.* **51,** 877–886.

Styles, P. (2005). A detailed study of the propagation and modelling of the effects of low frequency seismic vibration and infrasound from wind turbines, *Proc. 1st Int. Meeting on Wind Turbine Noise*, Berlin, Germany, 17–18 October 2005.

Vinet, J.-Y., V. Brisson , and S. Braccini (1996). Scattered light noise in gravitational wave interferometric detectors: Coherent effects, *Phys. Rev. D* **54,** 1276–1286.

Welch, P. (1967). A direct digital method of power spectrum estimation, *IBM J. Res. Dev.* **5,** 141.

Withers, M. M., R. C. Aster, C. J. Young, and E. P. Chael (1996). High-frequency analysis of seismic background noise as a function of wind speed and shallow depth, *Bull. Seismol. Soc. Amer.* **86,** 1507–1515.

Istituto Nazionale di Geofisica e Vulcanologia
Sezione di Pisa Via U
della Faggiola, 32-56126
Pisa, Italy
saccorotti@pi.ingv.it
davide.piccinini@ingv.it
(G.S., D.P.)

UCD School of Geological Sciences
University College Dublin
Belfield, Dublin 4
Ireland
lena.cauchie@gmail.com
(L.C.)

European Gravitational Observatory
Via E. Amaldi 56021
S.Stefano a Macerata
Cascina (PI), Italy
irene.fiori@ego-gw.it
(I.F.)

Manuscript received 23 July 2010